

Investigation of the Applicability of Droplet Transport for Top of the Line Corrosion Mitigation

Nicolas Jauseau⁽¹⁾, Fernando Farelas, Marc Singer⁽²⁾, Srdjan Nesic
Institute for Corrosion and Multiphase Technology
Department of Chemical and Biomolecular Engineering, Ohio University
342 West State Street
Athens, OH 45701, USA

ABSTRACT

The entrainment of liquid droplets, occurring in a limited range of gas and liquid flow conditions within the stratified flow region, could represent an effective way to transport a non-volatile liquid corrosion inhibitor through the gas phase and combat Top of the Line Corrosion (TLC). However, such an approach is only viable if the inhibitor can reach the top of the pipe and deposit at a rate higher than the local rate of condensing water can dilute it. This work presents a combined modeling and experimental methodology to determine the onset of droplet entrainment from the bottom and deposition at the top of the line. A modeling approach predicting the droplet entrainment onset is proposed and validated against new multiphase flow data recorded in a large scale flow loop, at operating conditions similar to those encountered in gas-condensate production facilities. Additionally, TLC experiments were performed in the same flow loop under simulated water condensation conditions to measure the actual corrosion at different rates of inhibiting droplet deposition. The results confirm that the droplet entrainment/deposition can effectively mitigate TLC when operating parameters are accurately controlled.

Key words: Droplet entrainment, droplet deposition, top of the line corrosion, inhibition.

INTRODUCTION

Top of the Line Corrosion (TLC) is a major challenge for many oil and gas operators because it causes pipe failures¹⁻⁶. It occurs in stratified flow regime in horizontal and near-horizontal pipelines under water condensing conditions. Continuous injection of standard chemical inhibitors is often used to mitigate TLC in production pipelines, but this method is only effective when the continuous water phase remains in contact with the pipe wall. Consequently, TLC mitigation remains a serious challenge as there is no straightforward way to transport the inhibitor present in the continuous liquid phase flowing at the bottom of the pipe to the top of the line. The use of concentrated inhibitor periodic batch treatments and deployment of volatile inhibitors are some of the currently proposed solutions, but they also present

¹ Present address: Kongsberg Digital Inc., 10777 Westheimer Rd, Suite 1200, Houston, TX 77042, USA.

² Corresponding author. E-mail: singer@ohio.edu.

many technical challenges, such as: selection of the proper volatile inhibitor package, verification of its effectiveness under TLC conditions, persistency of protection in batch treatment, selection of optimum batch frequency, etc.⁷⁻⁹

A change in the flow regime from stratified to non-stratified (e.g., annular or slug flow) could aid the continuous liquid phase to reach the top of the pipe and, thus, mitigate the problem, but may not be desirable from a flow assurance standpoint (i.e., mechanical stress on pipelines, separation issues at arrival facilities, erosion, etc.). However, inhibition may also be achieved in stratified flow when droplet entrainment is considered. At sufficiently high gas velocity, liquid droplets containing inhibitor can be sheared off from the bulk liquid phase at the bottom of the line and transported to the top via the gas phase. Once deposited at the top of the pipe, the inhibitor will still have to “compete” with the condensation of fresh water, which otherwise would dilute it and diminish its efficiency. Although this mitigation approach has been identified by several researchers¹⁰⁻¹¹, to the best of our knowledge, it has never been properly evaluated in a laboratory setting or in a field environment.

Operating conditions in gas-condensate pipelines (usually 14 – 40” in pipe diameter) feature medium to high pressures, where a gas phase characterized by high fluid densities ($\geq 60 \text{ kg/m}^3$) flows at relatively low gas velocities (5 – 15 m/s). Due to the complexity, cost and hazards, such field conditions are difficult to reproduce in a laboratory facility. On the other hand, droplet transport models that can be found in the open literature are based on laboratory data collected at much higher gas velocities (15 – 100 m/s) in low pressure environments (< 5 bar total pressure), which produce equivalent interfaces forces¹², proportional to gas density and velocity: $\rho_G U_G^2$. These large differences in gas velocity between the lab and field conditions affect not only the appearance and behavior of the stratified liquid/gas interface at the bottom of the line, but also the nature of dropwise condensation at the top, which makes the direct application of such lab results to the field difficult.

The present study addresses some of these limitations, by investigating the influence of droplet transport on carbon dioxide (CO₂) driven TLC. A model is developed to determine the onset of droplet entrainment and deposition at the top of the line. The modeling approach is supported by an experimental study performed in a large scale flow loop, focusing on the measurement of droplet entrainment and by using a heavy molecular weight gas to simulate high gas density seen in the field. A second experimental study, dedicated to TLC in water condensing conditions, is also carried out to verify the overall approach.

DEVELOPMENT AND VALIDATION OF THE DROPLET TRANSPORT MODEL

Modeling of entrainment onset

Mechanisms of entrainment onset

The entrainment of liquid droplets in a gas phase can be initiated by different mechanisms, such as: wave entrainment, bubble burst entrainment, and droplet impingement entrainment. The wave entrainment is the dominant entrainment mechanism in the present applications, with the other two being of secondary importance¹³⁻¹⁷. In the case of wave entrainment, the droplets are formed from disturbance waves (3D roll waves) created at the gas-liquid interface.

Wave entrainment can take various forms, such as wave coalescence, wave undercutting, and ripple wave shearing-off¹³. Among those, the ripple wave shearing-off, during which a wavelet at the wave crest is torn away and generates liquid droplets, is considered the dominant one¹⁶. At very low liquid loadings (low liquid Reynolds numbers Re_L), this wave entrainment mechanism does not occur. However, liquid droplets can still be formed by wave undercutting at sufficiently high gas velocities. In this case, a disturbance wave can be sheared-off into the gas core, and then, disintegrated into smaller liquid droplets¹³⁻¹⁴. Additionally, wave undercutting can occur at higher liquid flow rates in viscous fluids¹⁵. Therefore, to model the entrainment onset, the present study considers both forms, the ripple wave shearing-off and wave undercutting.

Definition of the entrainment onset

The occurrence of the entrainment onset is considered when some liquid droplets are torn from the gas-liquid interface, *i.e.*, when the atomization of liquid droplets occurs. In order to consider entrainment onset significant in horizontal pipes, one requires that the droplets are able to impinge on the top of the pipe. This is particularly important because it also defines the deposition of the liquid droplets in TLC, which has been observed previously in wet gas pipelines. The entrainment onset mechanism can be separated in three distinct regions. Below a critical liquid Reynolds number (low liquid flow rate), the superficial gas velocity required to initiate the droplet entrainment sharply increases reaching the entrainment limit¹⁸. At high liquid flow rates, no entrainment onset occurs below a critical gas velocity. Between these two limiting cases, the inception of droplet entrainment depends on both liquid and gas flow rates.

Model description

The modeling of entrainment onset transition follows the approach initially developed by Ishii and Grolmes, and later completed by Mantilla and coworkers¹⁹. Briefly, a force balance (Figure 1) is applied to a single wave, and consists of the drag force F_D , the surface tension force F_σ and the gravitational force F_g (equation 1).

$$F_D \geq F_\sigma + F_g \sin(\beta) \quad (1)$$

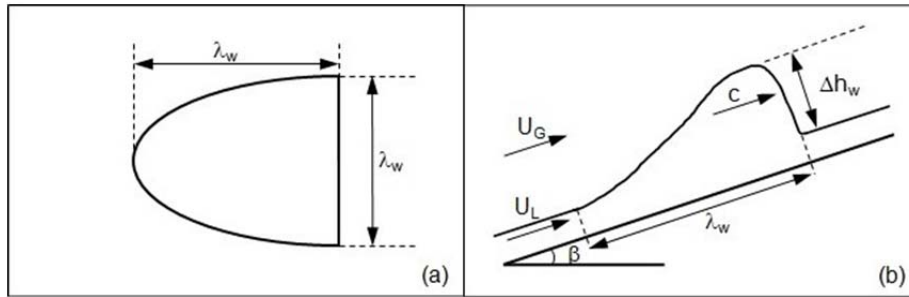


Figure 1: Top view (a) and side view (b) of a wave (adapted from Mantilla²²).

The drag force is defined as:

$$F_D = \frac{1}{2} C_D \lambda_w \Delta h_w \rho_G (U_G - U_L)^2 \quad (2)$$

C_D is the drag coefficient taken as $C_D = 0.95$ for irregular shapes. λ_w and Δh_w represent the length and height of the liquid wave, respectively.

The surface tension force is given by:

$$F_\sigma = C_S \lambda_w \sigma \quad (3)$$

C_S is the interfacial shape coefficient taken as $C_S = 0.77$ and corresponds to the average wave crest with a half elliptical base¹⁴.

The gravity force is calculated as:

$$F_g = \frac{\pi}{8} \lambda_w^2 \Delta h_w \rho_L g \sin(\beta) \quad (4)$$

By substituting equations (2) to (4) into equation (1), it yields:

$$C_D \Delta h_w \rho_G (U_G - U_L)^2 = 2C_S \sigma + \frac{\pi}{4} \lambda_w \Delta h_w \rho_L g \sin(\beta) \quad (5)$$

Following Ishii and Grolmes' recommendations, the interfacial shear stress at the wave crest τ_i is assumed to be proportional to the liquid film velocity:

$$\tau_i = C_w \mu_L \frac{U_L}{\Delta h_w} \quad (6)$$

C_w represents the effect of surface tension forces on the internal flow within the wave crest and can be expressed as a function of the liquid viscosity number N_μ , such as:

$$\frac{1}{3C_w} = \begin{cases} 11.78 N_\mu^{0.8} & , N_\mu \leq \frac{1}{15} \\ 1.35 & , N_\mu > \frac{1}{15} \end{cases} \quad (7)$$

where:

$$N_\mu = \mu_L \cdot \left[\rho_L \sigma \sqrt{\frac{\sigma}{(\rho_L - \rho_G)g}} \right]^{-1/2} \quad (8)$$

The interfacial shear stress τ_i can be calculated using either the liquid- or gas-interfacial friction factor, such as:

$$\tau_{Gi} = f_{Gi} \frac{\rho_G (U_G - U_L)^2}{2} \quad (9)$$

$$\tau_{Li} = f_{Li} \frac{\rho_L U_L^2}{2} \quad (10)$$

Using Hughmark²³, the liquid-interfacial friction factor τ_{Li} is defined as:

$$f_{Li} = \sqrt{1.962 / Re_L^{1/3}} \quad (11)$$

where:

$$Re_L = \frac{\rho_L D_L U_L}{\mu_L} \quad (12)$$

The gas-interfacial friction factor f_{Gi} was initially expressed as a constant. Mantilla accounted for the effect of pipe diameter since the friction factor is related to the relative roughness of the wave amplitude. A new correlation was developed and tuned with the help of a subset of randomly sampled experimental data collected in the present study for different gas-liquid mixtures of CO₂/water and SF₆ - CO₂/water²⁴. This subset of experimental data was not included in the set used for the validation of the model. The expression of f_{Gi} is shown below:

$$f_{Gi} = C_0 \left(\frac{T}{T^0} \right)^{C_1} \left(\frac{P}{P^0} \right)^{C_2} \left(\frac{MW_G}{MW_{air}} \right)^{C_3} \left(\frac{h_L}{D} \right)^{C_4} \quad (13)$$

where: $C_0 = 0.00140820$, $C_1 = -3.41122637$, $C_2 = 0.40052095$, $C_3 = 0.33121546$, $C_4 = -0.23537017$. MW_G and MW_{air} are the molecular weights of the gas phase and air, respectively ($MW_{air} = 28.97$ g/mol). Temperatures are expressed in degree K.

Assuming that $\tau_i = \tau_{Li}$ and using the shear stress continuity at the interface $\tau_{Li} = \tau_{Gi}$, substituting equations (9) and (10) into equation (6) yields the following expression:

$$\Delta h_w = 2C_w \frac{\mu_L}{\rho_L} \sqrt{\frac{\rho_L}{\rho_G} \cdot \frac{1}{f_{Li} f_{Gi}} \frac{1}{U_G - U_L}} = \frac{C_r}{U_G - U_L} \quad (14)$$

where:

$$C_r = 2C_w \frac{\mu_L}{\rho_L} \sqrt{\frac{\rho_L}{\rho_G} \cdot \frac{1}{f_{Li} f_{Gi}}} \quad (15)$$

Substituting equation (14) into the force balance equation (5) gives the following expression:

$$(U_G - U_L)^2 - 2 \frac{C_S \sigma}{C_r C_D \rho_G} (U_G - U_L) - \frac{\pi \lambda_w \rho_L g \sin(\beta)}{4 C_D \rho_G} \quad (16)$$

This 2nd degree polynomial has two possible solutions. The negative solution is discarded, while the positive solution represents the entrainment onset criterion:

$$U_G - U_L = \frac{C_S \sigma}{C_r C_D \rho_G} + \sqrt{\left(\frac{C_S \sigma}{C_r C_D \rho_G}\right)^2 + \frac{\pi \lambda_w \rho_L g \sin(\beta)}{4 C_D \rho_G}} \quad (17)$$

The liquid velocity is taken as being the wave celerity c , which can be expressed as a function of the pipe inclination²⁵:

$$c/U_{SL} = \begin{cases} 2.379X^{*-0.9}, & \beta = 0^\circ \\ 2.323X^{*-0.94}, & 10^\circ \leq \beta \leq 20^\circ \\ 1.942X^{*-0.91}, & \beta \geq 45^\circ \end{cases} \quad (18)$$

X^* is defined as the Froude numbers ratio between the liquid and gas phases:

$$X^* = \frac{Fr_{SL}}{Fr_{SG}} \quad (19)$$

$$Fr_{SL} = \sqrt{\frac{\rho_L U_{SL}^2}{(\rho_L - \rho_G) g D \cos \beta}} \quad (20)$$

$$Fr_{SG} = \sqrt{\frac{\rho_G U_{SG}^2}{(\rho_L - \rho_G) g D \cos \beta}} \quad (21)$$

The wave base length λ_w is expressed with the wave spacing L_w :

$$\lambda_w = L_w/2, \quad (22)$$

while the wave spacing is defined as:

$$L_w = 2\pi\sigma^{1/2} \left[\frac{(U_G - U_L)^2}{\frac{L_G + L_L}{\rho_G + \rho_L}} - (\rho_L - \rho_G)g \cos(\beta) \right]^{-1/2} \quad (23)$$

Both L_G and L_L are geometrical properties used in stratified flow and can be written as:

$$L_G = \frac{A_G}{dA_G/dh_G} \quad (24)$$

$$L_L = \frac{A_L}{dA_L/dh_L} \quad (25)$$

Limiting cases

At low liquid Reynolds numbers, the roll waves start disappearing due to a lower interfacial shear stress and a sudden increase in the critical velocity necessary to entrain the droplets¹⁴. For low viscosity fluids, this transition occurs at a critical liquid film Reynolds number $Re_{L,crit}$, which varies with the flow inclination in pipes:

$$Re_{L,crit} = 2 \quad \text{if } \beta = -90^\circ \quad (26)$$

$$Re_{L,crit} = 160 \quad \text{if } \beta = 0^\circ \text{ or } \beta = +90^\circ \quad (27)$$

Below $Re_{L,crit}$, the ripple wave shearing off mechanism does not occur. However, liquid droplets can still be formed by the wave undercutting mechanism when the liquid film Weber number We_L is in the range 17 – 22. The wave undercutting mechanism can be described by the following criterion using a Weber number of 22:

$$U_G - c = 1.5 \frac{\sigma}{\mu_L} \sqrt{\frac{\rho_L}{\rho_G} \cdot \frac{1}{Re_L}} \quad (28)$$

At high liquid Reynolds numbers ($Re_L > 5000$), the friction factor is assumed to remain constant; therefore, a value of $Re_L = 5000$ is used in equation (11).

Experimental study of droplet transport

Entrainment onset data found in the literature are scarce and often measured at operating conditions that are not representative for gas-condensate transportation pipelines (low gas density, high gas velocity). Therefore, an experimental setup was developed in this study to generate data as close as possible to the conditions observed in field operations. The experimental study involved a measurement of the droplet transport using visual observations at the transparent wall of the pipe (non-intrusive) and by using a borescope (camera) inserted within the pipe (intrusive).

Equipment

The experimental work was carried out in a large scale wet gas flow loop, which was designed to study both droplet transport and CO₂ corrosion under two-phase gas-liquid flow conditions (Figure 2). The apparatus is a 0.102 m (4 in) pipe diameter 30 m long flow loop entirely made of stainless steel UNS S31600, except for the test section; for droplet transport experiments, this latter consisted of a 5 m long transparent acrylic pipe to visualize and record the flow regime occurring in the loop.

The gas phase could be either pure CO₂ or a CO₂/sulfur hexafluoride (SF₆) mixture. The inert gas SF₆, characterized by a high molecular weight, was used to artificially increase the density of the gas stream in order to closely mimic conditions existing in pressurized gas production facilities. The gas flow rate, supplied by a gas blower, had a maximum capacity of 190.7 SCFM (0.09 Sm³/s) and was measured using a 5 psi differential pressure transducer installed around a vortex flow meter. Deionized (DI) water was used as the liquid phase whose flow rate was controlled by a gear pump, which could deliver up to 9.5 gal/min (0.6·10⁻³ m³/s).

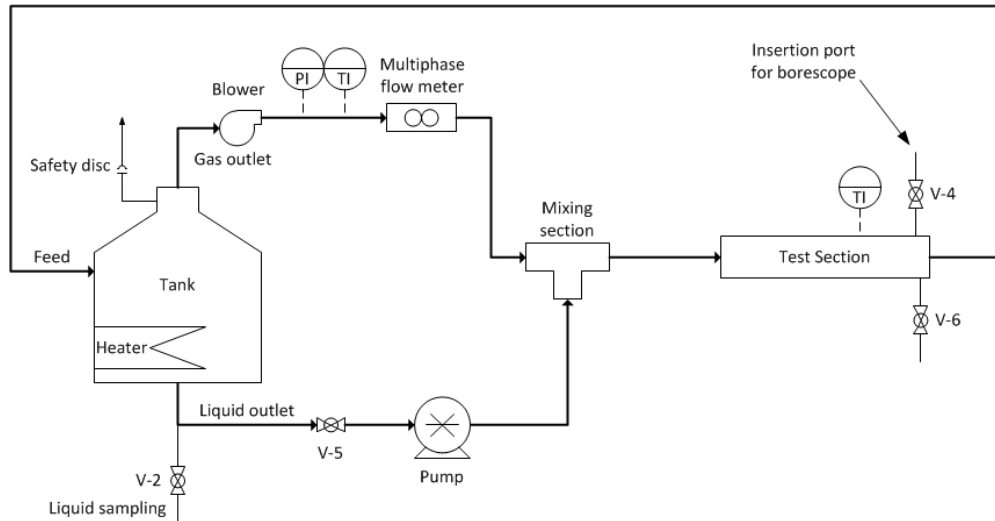


Figure 2: Process and flow diagram of the wet gas flow loop (experimental droplet transport).

A slab was introduced at the mixing location between the gas and liquid phases to generate a fully segregated flow while minimizing liquid splashing (Figure 3); it should be noted that the intrusive slab did not generate a significant pressure drop in the flow loop. The test section was located at 60 L/D downstream of the mixing section. The instrumentation included pressure and temperature measurement devices, and a high pressure borescope mounted on the pipe to record the onset of droplet entrainment (Figure 4). The borescope tip was positioned as close as possible to the top of the pipe, so that the droplet entrainment could be directly observed when droplets hit the lens of the borescope.

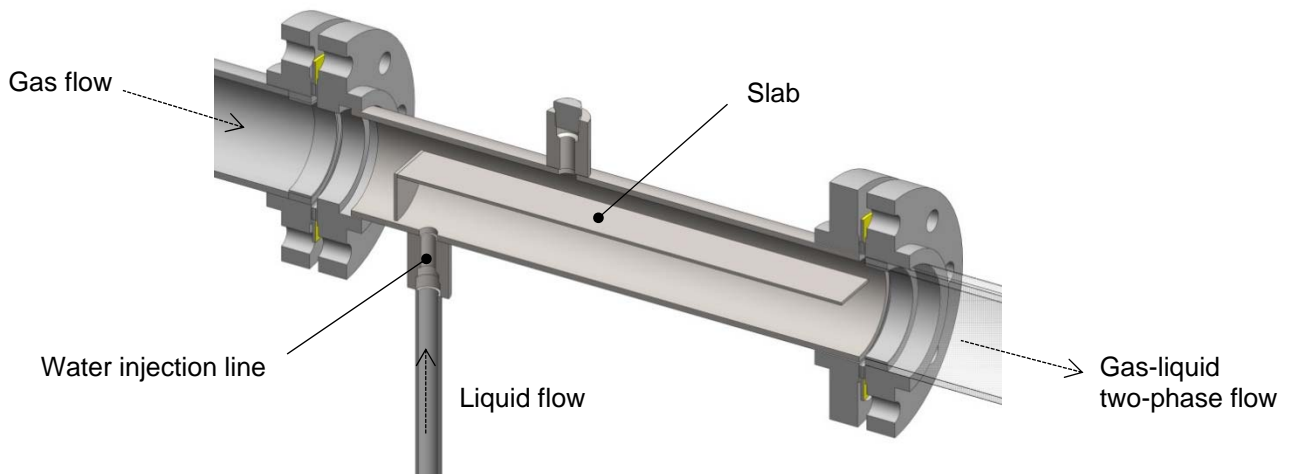


Figure 3: Cross sectional view of the gas-liquid mixing section. (Courtesy of Cody Shafer, Institute for Corrosion and Multiphase Technology)

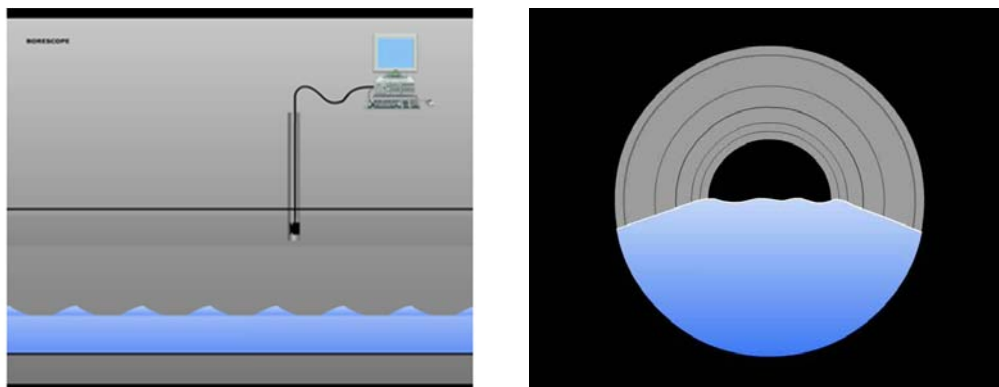


Figure 4 : Boreoscope set up in the test section of the large scale flow wet gas loop (left side) and cross sectional representation of a two-phase gas-water flow inside the pipe (right side).

Methodology

The criterion to determine the onset of droplet entrainment in the pipe was that at least one liquid droplet should hit the boreoscope lens every 10 seconds. In such conditions and by considering the size of the droplets and the number of “hits” per surface area and per time, the corresponding deposition rate at the top of the line was roughly estimated to 0.001-0.01 mL/m²/s.

Prior to the experiments, 300 L of DI water were introduced in the tank and sparged with CO₂ for four hours to remove most of the O₂ and N₂ from the system. The composition of the gas stream was maintained constant by monitoring the partial pressure of each gas (*i.e.*, CO₂ and SF₆) and carefully recorded since an increase in SF₆ concentration in the gas stream increased the gas density. Then, the boreoscope was introduced in the test section; the insertion port was carefully sealed to avoid any gas leak. During each experiment, the liquid flow rate was set to a constant value whereas the gas flow rate was slowly increased until the droplet entrainment onset was achieved. Between each gas rate increment, a sufficient amount of time (usually 15-30 min) was dispensed to make sure the flow loop truly reached steady state conditions. Once the entrainment onset was observed on the boreoscope, the partial pressures, temperatures, and flow rates were recorded.

Using a constant gas composition, twenty independent series of measurements were performed by varying the superficial liquid velocity from 0.004 to 0.072 m/s (see experimental conditions in Table 1). Using SF₆ instead of methane as a gas phase meant that only 5 bara of SF₆ gas could approximate the same density as 50 bara of methane due to the molecular weight difference ($MW_{SF_6} = 146$ g/mol vs. $MW_{CH_4} = 16$ g/mol). For consistency, the results are displayed as a function of the methane equivalent pressure $P_{CH_4}^{eq}$ (also noted *eq* P_{CH_4}) in the rest of the text.

Table 1: Test matrix for droplet transport experiments.

Parameters	Conditions
Gas phase	SF ₆ / CO ₂ SF ₆ concentration in gas stream: 0 to 72 mol%
Liquid phase	DI water
Superficial gas velocity (m/s)	5 – 12
Superficial liquid velocity (m/s)	0.004 – 0.072
CH ₄ equivalent pressure (bara)	4.4 – 35
Temperature (°C)	25 – 40

Results

The experimental results in Figure 5 present a subset of the entrainment onset data collected in this study, expressing the critical superficial gas velocity $U_{SG,crit}$ above which droplets start to deposit at the top of the line as a function of the equivalent CH_4 pressure. At the lowest tested pressure ($P_{CH_4}^{eq} = 4.7$ bara), the onset of droplet entrainment was reached around $U_{SG,crit} = 10.3 \pm 0.2$ m/s at low liquid flow rate ($U_{SL} = 0.014$ m/s) and $U_{SG,crit} = 8.8 \pm 0.2$ m/s at higher liquid flow rate ($U_{SL} = 0.072$ m/s). As the liquid flow rate increases, the liquid holdup increases in the pipe and decreases the distance between the top of the pipe and the gas-liquid interface (we reasonably assumed a horizontal gas-liquid interface here). In turn, the cross sectional area of the gas phase decreases and the in situ gas velocity slightly increases, allowing the droplet entrainment onset to occur at a lower gas velocity.

As the total pressure (*i.e.*, the gas density) increases, the interfacial shear stress between the gas and the liquid phase increases as well. Ripples and waves present at the gas-liquid interface can be further torn away to generate droplets. In a 4 in pipe, the onset of droplet entrainment was observed for superficial gas velocities in the range of 6 – 11 m/s at equivalent CH_4 pressure ranging from 4 to 35 bara.

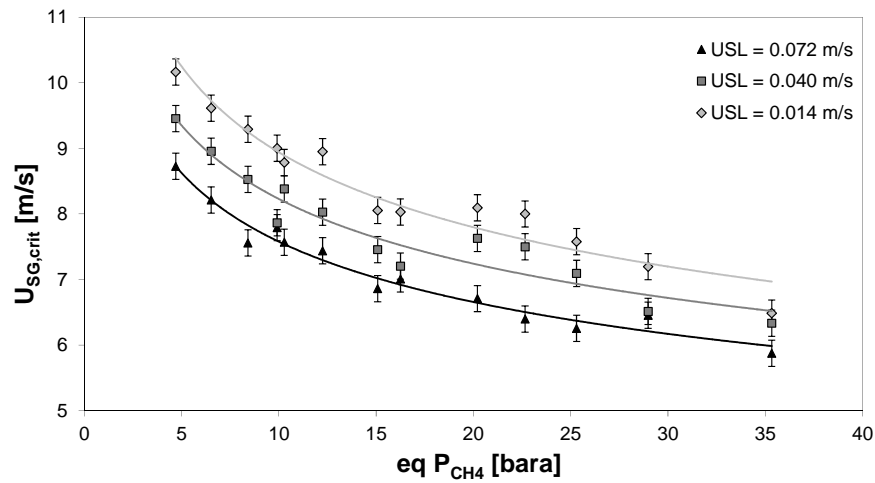


Figure 5: Droplet entrainment onset at the top of the pipe as a function of total pressure and superficial liquid velocity U_{SL} .

Entrainment model validation

The performance and accuracy of the droplet transport model were evaluated using statistical tools (Table 2), such as the average percent error ε_1 , average absolute percent error ε_2 , and percent standard deviation ε_3 . These parameters require the determination of relative error e_R , representing the deviation of predicted value (X_{pred}) from the experimental observation (X_{exp}).

Table 2: Statistical tools used for the model validation.

Statistical variable	Equation	Statistical variable	Equation
Relative error	$e_R = \frac{X_{pred} - X_{exp}}{X_{exp}}$	Average absolute percent error	$\varepsilon_2 = \frac{1}{n} (\sum_{i=1}^n e_{R,i} \times 100)$
Average percent error	$\varepsilon_1 = \frac{1}{n} (\sum_{i=1}^n e_{R,i} \times 100)$	Percent standard deviation	$\varepsilon_3 = \sqrt{\frac{\sum_{i=1}^n (e_{R,i} \times 100 - \varepsilon_1)^2}{n-1}}$

A total of 258 entrainment onset measurements were collected in this study using different gas phase SF_6/CO_2 compositions. Additionally, entrainment onset data from literature was included in the

database (Table 3); this additional data were measured at near atmospheric pressure, featuring much higher gas velocities and lower gas densities compared to the present study. Overall, the entrainment onset database totaled 303 measurements. A random subsample of 33 was used for tuning the model; this subsample was not included in the model validation. Therefore, 270 measurements were finally used for model validation (Table 3). Based on statistical analysis tools (Table 2), the relative errors of the model predictions were calculated as the difference between the predicted and experimental superficial gas velocity at a given superficial liquid velocity, then averaged for each dataset and the entire database (Table 4). The model predicted most accurately the present study's data (2.9%), with consistent prediction errors (3.8 %) regardless of the gas phase composition. A comparison between the predicted and measured entrainment onset is shown on a flow regime map (Figure 6), using two different gas compositions in the gas-liquid mixtures (pure CO₂ and mixture CO₂/SF₆).

Table 3: Experimental data used for the entrainment onset model validation.

Authors	Data points	Fluids	Pipe diameter (m)
Andritsos (1986)	14	Air / Water	0.025, 0.095
Andritsos (1986)	10	Air / Water-glycerine	0.025, 0.095
Mantilla (2008)	14	Air / Water	0.049, 0.152
Mantilla (2008)	4	Air / Water-glycerine	0.049
Mantilla (2008)	3	Air / Water-butanol	0.049
This study	97	CO ₂ / Water	0.095
This study	161	SF ₆ -CO ₂ / Water	0.095

Table 4: Performance evaluation of the entrainment onset model.

Authors	Data points	Statistics		
		ε_1 (%)	ε_2 (%)	ε_3 (%)
This study	225	0.2	2.9	3.8
Andritsos (1986)	24	-9.9	26.7	32.6
Mantilla (2009)	21	10.9	22.9	28.4
All data	270	0.1	6.6	13.4

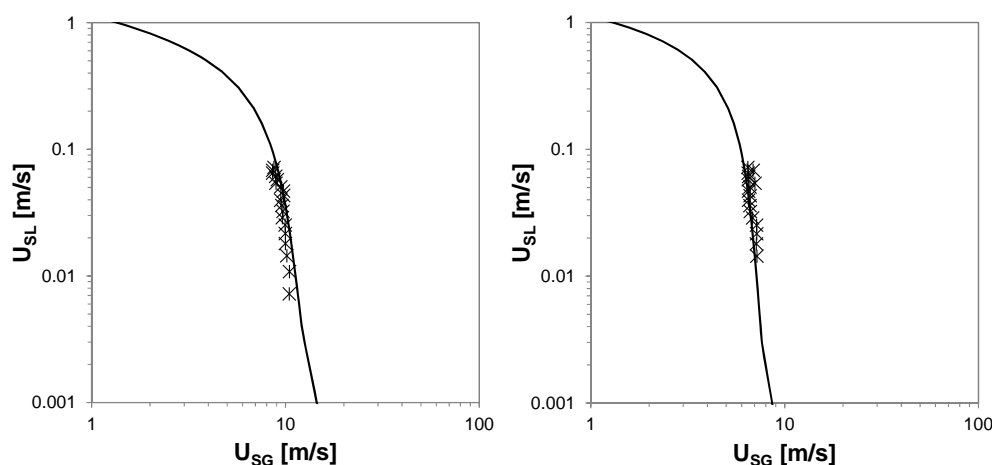


Figure 6: Predicted (line) vs. measured (markers) entrainment onset gas velocities for CO₂-water mixture ($P_{CH_4}^{eq} = 4.7$ bara, $T = 27.4$ °C) (left) and CO₂/SF₆-water mixture with 72 mol% SF₆ ($P_{CH_4}^{eq} = 35.3$ bara, $T = 29.3$ °C) (right).

A similar comparison is made for superficial gas velocity at the entrainment onset at different gas-liquid mixtures (Figure 7). The majority of data points fall within the $\pm 20\%$ deviations from the ideal agreement. The model agrees better with the entrainment onset observed with the borescope camera (present work and Mantilla) compared to the entrainment onset detected visually, from outside the pipe (Andritsos²⁶).

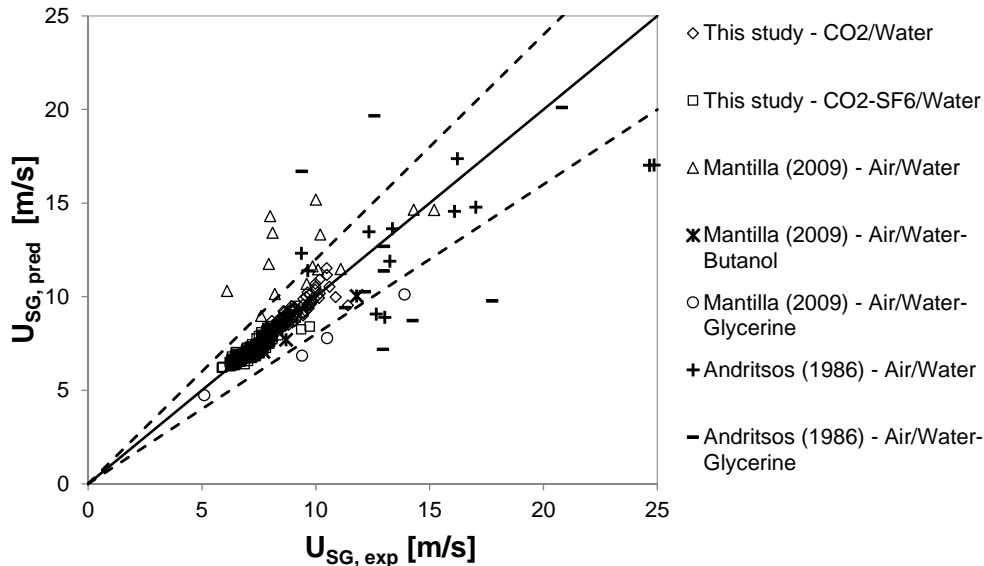


Figure 7: Predicted vs. experimental entrainment onset expressed as superficial gas velocity U_{SG} . Dashed lines represent the $\pm 20\%$ deviations from the 1:1 line.

Comparisons between the model and Mantilla data exhibited a slight overprediction (+10.9%) and an average absolute percent error of 22.9%. Unlike the entrainment onset criterion used in this study (see Methodology), Mantilla’s entrainment onset was defined as “a droplet hitting the top of the pipe every 5 to 10 seconds”²². This difference in experimental data between the two studies may explain the overprediction of the droplet entrainment onset when considering air-water measurements (Figure 7). The large scattering observed with viscous fluid data (liquid phase as water-glycerine) suggests that the present model does not account for the effect of viscosity very well; for more accurate entrainment onset predictions, only measurements from fluids with liquid viscosities less than $5 \cdot 10^{-3}$ Pa·s should be used to validate this model.

INHIBITION OF TOP OF THE LINE CORROSION BY DROPLET TRANSPORT

A set of corrosion experiments was performed under high pressure and high temperature conditions in the large scale wet gas flow loop to validate the concept of droplet transport as an effective TLC mitigation method. A corrosion inhibitor was injected in the bulk liquid phase under stratified flow conditions, with or without droplet entrainment present in the gas phase. TLC rates were measured on steel specimens installed in a custom designed cooled TLC test section.

Experimental procedure

The experimental corrosion study was performed on the same large scale flow loop used for the determination of droplet entrainment, with the test section modified to suit high pressure and high temperature conditions. A process and flow diagram of the flow loop used for the corrosion experiments is shown in Figure 8. The flow loop was equipped with two identical test sections, designed to investigate TLC. The test sections were 4 in (0.102 m) inner diameter (ID) pipe made of UNS S31600

and equipped with eight 2 in (0.051 m) ID probe ports through which corrosion measurements devices could be inserted (Figure 9). Four of these ports were located at the bottom of the pipe (6 o'clock position) while the other four ports were located at the top of the pipe (12 o'clock position). Copper coils were wrapped around the pipe and used to circulate cooling water. The water condensation rate was measured using a condensed water collector located downstream of the test section. The gas and inner pipe wall temperatures were measured continuously during the experiments. A more detailed description of the experimental setup can be found elsewhere¹.

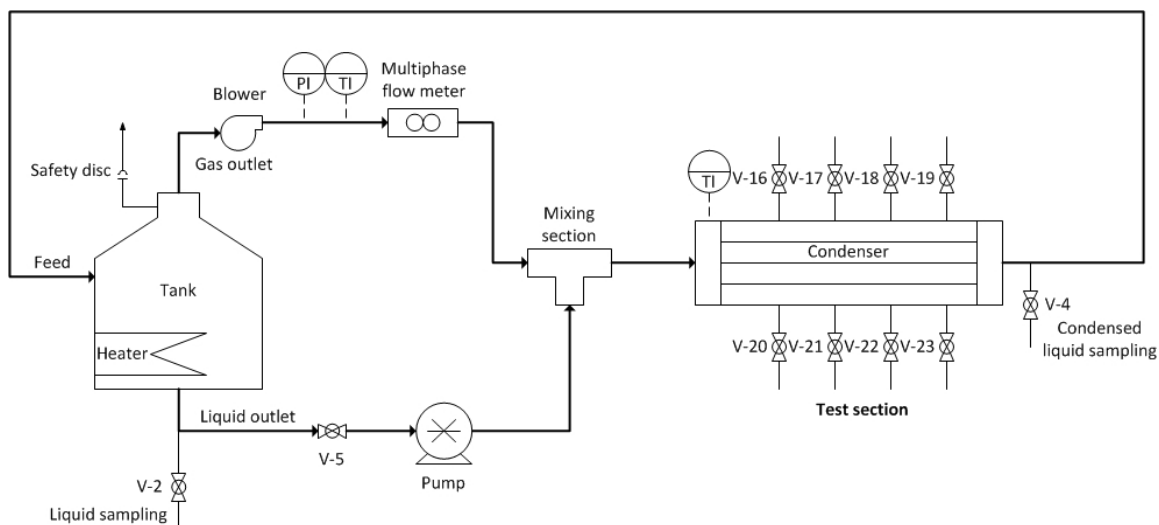


Figure 8: Process and flow diagram of the flow loop for the HP/HT corrosion experimental study.

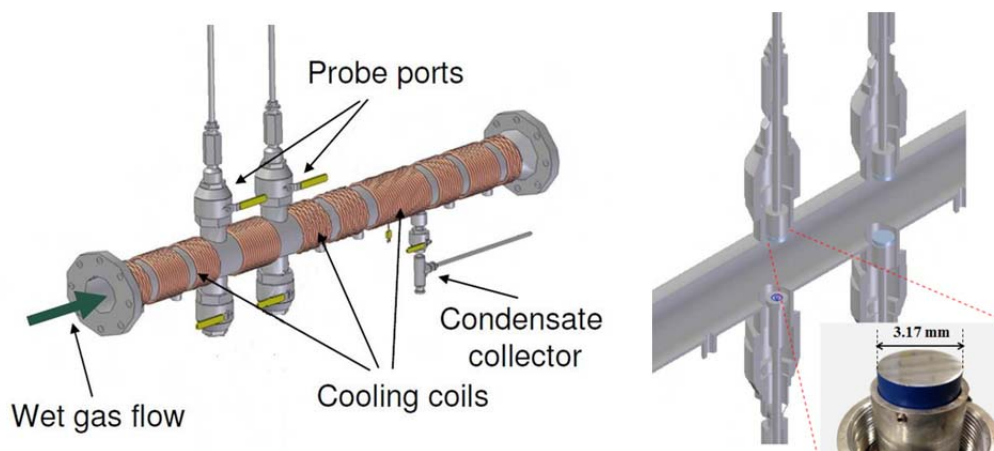


Figure 9: Schematic of the test section in HP/HT corrosion flow loop (left view); cross section of the corrosion probe with its mounted corrosion sample (right view).

For each test, the liquid phase consisted of an aqueous solution containing 1 wt% sodium chloride (NaCl), deoxygenated with CO₂ prior to the tests (O₂ concentration around 20 ppb). The pH of the solution was set constant to 5.9 and controlled by addition of sodium hydroxide to decrease the aggressiveness of the environment and enhance the corrosion inhibitor efficiency. The gas phase consisted of a CO₂/SF₆ mixture with 70 mol% SF₆; the equivalent methane pressure was 28.5 bara. The liquid phase in the tank was heated to the required temperature using immersion heaters. The gas blower and the liquid pump were used to get the desired gas and liquid flow rates, respectively.

The corrosion samples used in experiments were carbon steel (CS) UNS K03014 with a 7.2 cm² exposed area (Figure 9, right hand side). CS specimens were polished with 220, 400 and 600 grit silicon carbide paper under a flush of isopropanol before any testing. During the experiment, two samples at the bottom and three at the top of the pipe were flush mounted in the test section.

The corrosion inhibitor was selected based on its past demonstrated efficiency against bottom of the line corrosion^{20,21} and consisted of an imidazoline based chemical (10% CH₃COOH, 13% CH₄H₉OCH₂CH₂OH, 24% Tall oil fatty acid / Diethylene triamine imidazoline, balance water). A non-volatile inhibitor was preferred in this study because a mechanical mass transfer by droplet entrainment was the only intended way of transporting the inhibitor to the top of the pipe.

Three independent tests (A, B and C) were conducted using different superficial gas velocities and inhibitor concentrations to measure both bottom of the line corrosion (BLC) and TLC. In test A, the superficial liquid and gas velocities were selected to ensure stratified flow regime, while limiting any significant droplet entrainment in the pipe. The liquid droplets eventually present at the top of the pipe would only result from the condensation of water vapor due to the cooling of the pipe wall. In tests B and C, an increase in superficial gas velocity from 3.2 to 6.9 m/s changed the flow regime from stratified without droplet entrainment to stratified with droplet entrainment and deposition at the top of the pipe. In test C, 300 ppm of corrosion inhibitor was injected to evaluate the inhibition effect on both BLC and TLC. Details about the operating conditions used during those tests are given in Table 5.

Table 5: Test conditions for TLC experiments.

Parameters	Conditions		
Gas temperature (°C)	70 – 72		
Gas composition (mol%)	70.2 (SF ₆) + CO ₂ (29.8)		
Equivalent CH ₄ pressure (bara)	28.5		
NaCl solution (wt)	1		
Solution pH	5.9		
Test duration (day)	2		
	Test A	Test B	Test C
Superficial liquid velocity (m/s)	0.06	0.06	0.06
Superficial gas velocity (m/s)	3.2	6.9	6.9
Inhibitor concentration (ppm)	0	0	300
Flow pattern	Stratified	Stratified	Stratified
Droplet entrainment in the pipe	no	YES	YES
In-situ liquid velocity (m/s)	0.58	1.23	1.23
Predicted water condensation rate (mL/m ² /s)	0.14	0.25	0.25
Predicted droplet deposition rate (mL/m ² /s)	0	2.16	2.16

Experimental results

Corrosion rate analysis

Corrosion rates in this experimental study were measured using the weight loss method on the samples located at both bottom and top of the line for the tests A, B and C (Figure 10). At the bottom of the pipe, the baseline test (Test A) exhibited a high corrosion rate of 8.4 mm/y due to the combination of high temperature conditions and the absence of corrosion inhibitor (Figure 10). The gas flow rate was doubled from test A to test B and, consequently, the corrosion rate increased to a higher value of 11.7

mm/y. The higher superficial gas velocity increased the in situ aqueous velocity (from 0.58 to 1.23 m/s) due to slippage, which, in turn, enhanced the transport of corrosive species to the steel surface. Under the same operating conditions, the corrosiveness of the medium was mitigated by the addition of 300 ppm of inhibitor (Test C); the bottom of the line corrosion rate drastically dropped to 0.3 mm/y, which represents an inhibition efficiency of 97.4%.

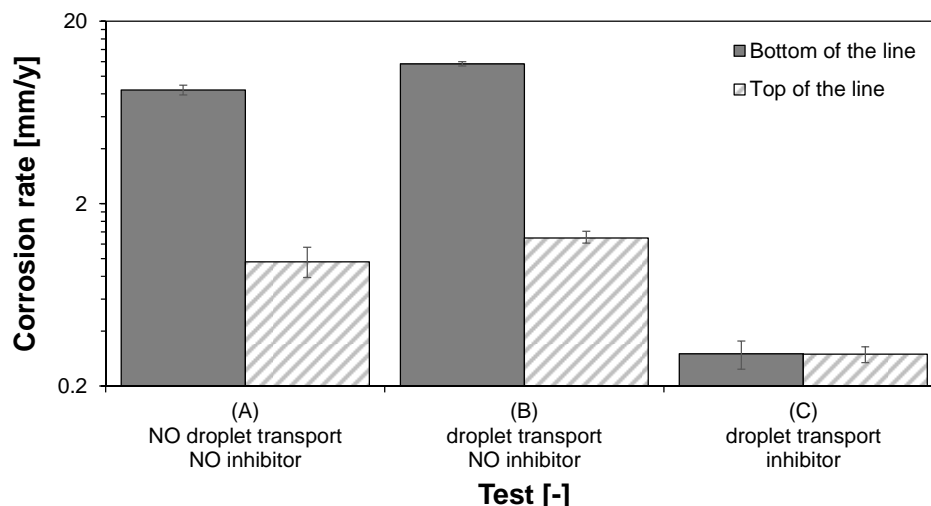


Figure 10: BLC and TLC rates in absence/presence of droplet transport and corrosion inhibitor.

The measured TLC rates show the same trend as the measured BLC rates (Figure 10). The baseline test (Test A) exhibited a TLC rate of 0.96 mm/y due to the sole presence of condensed water at the top of the pipe. More corrosive conditions were experienced at higher gas velocity with significant droplet transport, yielding a corrosion rate of 1.3 mm/y (Test B). A higher superficial gas velocity promoted not only the entrainment and deposition of water droplets at the top of the pipe (2.16 mL/m²/s), but also enhanced heat transfer at the pipe wall leading to higher water condensation rates (0.25 mL/m²/s). The injection of 300 ppm of corrosion inhibitor in test C mitigated the CO₂ corrosion attack at the top of the line with a TLC rate dropping to 0.3 mm/y, which is the same as the inhibited BLC rate since the inhibitor concentration at the top and bottom of the line was then similar. In the absence of a volatile corrosion inhibitor, the inhibition was only possible by utilizing the mechanical entrainment of liquid droplets to transport the chemical inhibitor to the top of the pipe. This method can only be effective to mitigate TLC as long as the droplet deposition rate remains higher than the water condensation rate as it was demonstrated in the present test.

Surface analysis

A SEM surface analysis of the steel samples exposed to BLC and TLC conditions was conducted after tests B and C (Figure 11). In the absence of corrosion inhibitor, the BLC specimen showed a “cracked” Fe₃C layer typically observed in CO₂ corrosion (Figure 11a). In the presence of corrosion inhibitor, the BLC specimen still had signs of the polishing marks, signifying a less aggressive corrosion medium (Figure 11b). Crystals of iron carbonate FeCO₃ were observed on the TLC specimen in an un-inhibited environment (Figure 11c). No FeCO₃ was observed on the TLC specimen surface (Figure 11d), which confirms the effective transport of corrosion inhibitor to the top of the pipe by a mechanism of droplet entrainment/deposition.

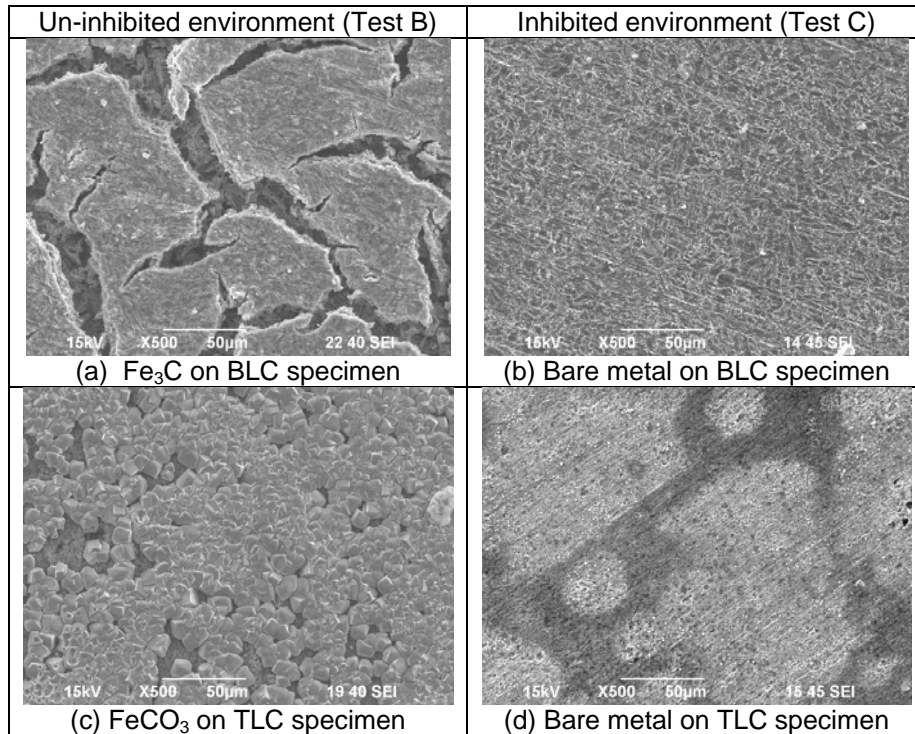


Figure 11: SEM images of the surface of the TLC and BLC specimens after exposure to a corrosive environment.

CONCLUSIONS

This study investigated the entrainment and deposition of liquid droplets in a gas phase as a potential solution to transport a non-volatile corrosion inhibitor to the top of the pipe. A mechanistic model was developed to predict the onset of droplet entrainment in horizontal and near-horizontal pipes under gas-liquid two-phase conditions. The model was further validated using newly acquired data from a large scale flow loop mimicking operating conditions similar to those encountered in wet gas transportation lines.

Using controlled multiphase flow and water condensation conditions, corrosion experimentation in a high pressure high temperature large scale flow loop additionally demonstrated that CO₂ top of line corrosion could be mitigated by transporting a non-volatile corrosion inhibitor to the top by droplet entrainment.

ACKNOWLEDGEMENTS

The authors would like to acknowledge the sponsors of the Top of the Line Corrosion JIP and the technical support from the Institute for Corrosion and Multiphase Technology at Ohio University.

GLOSSARY

Latin symbols

c : Wave celerity (m/s)
 CR : Corrosion rate (mm/y)
 D : Diameter (m)
 e_R : Relative error (-)

F : Force (N)
 f : Fanning friction factor (-)
 g : Gravity constant ($g = 9.81 m/s^2$)
 h : Height (m)
 L : Length (m)

MW : Molecular weight (g/mol)
 P : Pressure (kPa)
 T : Temperature ($^{\circ}C$)
 U : Velocity (m/s)
 X^* : Froude number ratio (-)

Greek symbols

β : Pipe inclination angle (degree)
 ε_1 : Average relative error (%)
 ε_2 : Absolute average relative error (%)
 ε_3 : Standard deviation of relative error (%)
 λ : Length (m)
 μ : Dynamic viscosity (kg/m/s)
 ρ : Density (kg/m³)
 σ : Surface tension (N/m)
 τ : Shear stress (Pa)

Superscripts

0 : Standard conditions (101.3 kPa, 15.6 $^{\circ}C$)

Subscripts

$crit$: Relating to entrainment onset conditions
 D : Relating to the drag force
 exp : Relating to experimental measurements
 G : Based on the gas phase
 g : Relating to the gravity force
 i : Relating to the gas-liquid interface
 L : Based on the liquid phase
 $pred$: Relating to predicted values
 S : Relating to the interfacial shape
 SG : Based on the superficial gas
 SL : Based on the superficial liquid
 w : Relating to the wave
 σ : Relating to the surface tension force

Dimensionless numbers

Fr : Froude number
 N_{μ} : Viscosity number
 Re : Reynolds number

REFERENCES

1. M. Singer, D. Hinkson, Z. Zhang, H. Wang, S. Nestic, CO₂ Top-of-the-Line Corrosion in Presence of Acetic Acid: A Parametric Study. *Corrosion* 2013, 69, 7, 719-735.
2. Pugh D., Asher S., Cai J., Sisak W., Pacheco J., Ibrahim F. and Wright E., Top-of-line corrosion mechanisms for sour wet gas pipelines, *CORROSION* 2009, paper no. 9285 (Atlanta, GA: NACE, 2009).
3. Y. Gunaltun, D. Supriyataman, A. Jumakludin, Top of the Line Corrosion in Multiphase Gas Line. A Case History, *CORROSION* 1999, paper no. 36 (Houston, TX: NACE, 1999).
4. J.R. Piccardino, M. Stuvik, Y. Gunaltun, T. Pornthep, Internal Inspection of Wet Gas Line Subject to Top of Line Corrosion, *CORROSION* 2004, paper no. 5354 (Houston, TX: NACE, 2004).
5. M. Edwards, B. Cramer, Top of the Line Corrosion – Diagnostic, Root Cause Analysis and Treatment, *CORROSION* 2000, paper no. 72 (Houston, TX: NACE, 2000).
6. Y. Gunaltun, Design of Multiphase Offshore Pipelines with High Risk of Sweet Top of the Line corrosion, *CORROSION* 2013, paper no. 2290 (Orlando, FL: NACE, 2013).
7. Z. Belarbi, F. Farelas, M. Singer, S. Nestic, Role of Amines in the Mitigation of CO₂ Top of the Line Corrosion. *Corrosion* 2016, 72, 10, 1300-1310.
8. Z. Belarbi, T.N. Vu, F. Farelas, M. Singer, S. Nestic, Thiols as Volatile Corrosion Inhibitors for Top-of-the-Line Corrosion, *Corrosion* 2017, 73, 7, 892-899.
9. Y. Gunaltun, T.E. Pou, M. Singer, C. Duret, S. Espitalier, Laboratory Testing of Volatile Corrosion Inhibitors. *CORROSION* 2010, paper no. 10095 (San Antonio, TX: NACE, 2010).
10. Z. Zhang, A Study of Top of the Line Corrosion Under Dropwise Condensation, PhD dissertation, Ohio University, Athens, OH, 2008.
11. M. Singer, (2017). *Part III: Corrosion Mechanisms: Current Knowledge, Gaps and Future Research Top-of-Line corrosion*, in "Trends in Oil and Gas Corrosion Research and Technologies". 1st edition. edited by A. M. El-Sherik, Woodhead Publishing.
12. D. Tayebi, S. Nuland, P. Fuchs, Droplet Transport in Oil/Gas and Water/Gas Flow at High Gas Densities. *Int. J. Multiphase Flow* 2000, 26, 741-761.

13. H. Han, K.S. Gabriel, A Numerical Study of Entrainment Mechanism in Axisymmetric Annular Gas-Liquid Flow. *J. Fluids Eng. Trans. ASME* 2007, 129, 293-301.
14. M. Ishii, M.A. Grolmes, Inception Criteria for Droplet Entrainment in Two-Phase Concurrent Film Flow. *AIChE J.* 1975, 21, 308-318.
15. I. Kataoka, M. Ishii, K. Mishima, Generation and Size Distribution of Droplet in Annular Two-Phase Flow. *J. Fluids Eng. Trans. ASME* 1983, 105, 230-238.
16. D.E. Woodmansee, T.J. Hanratty, Mechanism for Removal of Droplets from Liquid Surface by Parallel Air Flow. *Chem. Eng. Sci.* 1969, 24, 299-307.
17. J.J. Van Rossum, Experimental Investigation of Horizontal Liquid Films: Wave Formation, Atomization, Film Thickness. *Chem. Eng. Sci.* 1959, 11, 35-52.
18. G.F. Hewitt, N.S. Hall-Taylor, *Annular Two-Phase Flow*, 1st ed. (Oxford, UK: Pergamon Press, 1970).
19. I. Mantilla, L.E. Gomez, R.S. Mohan, O. Shoham, G.E. Kouba, R. Roberts. Modeling of Liquid Entrainment in Gas in Horizontal Pipes, ASME Fluids Engineering Division Summer Conference, paper no. FEDSM2009-78459 (New York, NY: American Society of Mechanical Engineers, 2009).
20. Y. Ding, B. Brown, D. Young, S. Nestic, M. Singer, Effect of Temperature on Adsorption Behavior and Corrosion Inhibition Performance of Imidazoline-Type Inhibitor, CORROSION 2017, paper no. 9350 (Phoenix, AZ: NACE, 2017).
21. S. Hassani, J. Huang, A.C. Victor, B. Brown, M. Singer, Inhibited Under-Deposit CO₂ Corrosion: Small Particle Silica Sand and Eicosane Paraffin Deposits, CORROSION 2017, paper no. 9564 (Phoenix, AZ: NACE, 2017).
22. I. Mantilla, Mechanistic Modeling of Liquid Entrainment in Gas in Horizontal Pipes. Ph.D. Dissertation, University of Tulsa, Tulsa, OK, 2008.
23. G.A. Hughmark, Film Thickness, Entrainment, and Pressure Drop in Upward Annular and Dispersed Flow. *AIChE J.* 1973, 19, 1062-1065.
24. N. Jauseau, Multiphase Flow Effects on Naphthenic Acid Corrosion of Carbon Steel. Ph.D. dissertation, Ohio University, Athens, OH, 2012.
25. A. Al-Sarkhi, C. Sarica, K.L. Magrini, Inclination Effects on Wave Characteristics in Annular Gas-Liquid Flows. *AIChE J.* 2012, 58, 1018-1029.
26. N. Andritsos, Effect of Pipe Diameter and Liquid Viscosity on Horizontal Stratified Flow. Ph.D. Dissertation, University of Illinois, Urbana-Champaign, IL, 1986.